

Anisotropic conductance at improper ferroelectric domain walls

D. Meier^{1,2*}, J. Seidel^{1,3,4*}, A. Cano⁵, K. Delaney⁶, Y. Kumagai⁷, M. Mostovoy⁸, N. A. Spaldin⁷, R. Ramesh^{1,2,3} and M. Fiebig⁷

Transition metal oxides hold great potential for the development of new device paradigms because of the field-tunable functionalities driven by their strong electronic correlations, combined with their earth abundance and environmental friendliness. Recently, the interfaces between transition-metal oxides have revealed striking phenomena, such as insulator-metal transitions, magnetism, magnetoresistance and superconductivity^{1–9}. Such oxide interfaces are usually produced by sophisticated layer-by-layer growth techniques, which can yield high-quality, epitaxial interfaces with almost monolayer control of atomic positions. The resulting interfaces, however, are fixed in space by the arrangement of the atoms. Here we demonstrate a route to overcoming this geometric limitation. We show that the electrical conductance at the interfacial ferroelectric domain walls in hexagonal ErMnO₃ is a continuous function of the domain wall orientation, with a range of an order of magnitude. We explain the observed behaviour using first-principles density functional and phenomenological theories, and relate it to the unexpected stability of head-to-head and tail-to-tail domain walls in ErMnO₃ and related hexagonal manganites¹⁰. As the domain wall orientation in ferroelectrics is tunable using modest external electric fields, our finding opens a degree of freedom that is not accessible to spatially fixed interfaces.

There have been a number of recent reports of unexpected electrical properties at ferroelectric domain walls, particularly in multiferroic materials with their simultaneous ferroelectric and magnetic order^{11,12}. For example, high local electrical conductance was measured at ferroelectric domain walls in BiFeO₃, whereas the 180° domain walls in hexagonal YMnO₃ were found to have higher resistivity than the bulk material^{10,13,14}. It is known that such multiferroics often have unconventional mechanisms driving the formation of their ferroelectric domains and domain walls, which are distinct from those of textbook ferroelectrics such as BaTiO₃ (ref. 15). Multiferroics are therefore a likely source for novel domain and domain-wall properties. In the specific case of the hexagonal manganite multiferroics studied here, the primary symmetry-lowering order parameter is a unit-cell-tripling distortive mode and the subsequent geometrically driven ferroelectricity is improper^{16,17}. The orientation of the resulting spontaneous polarization is set by the tripling mode, which does not itself introduce a ferroelectric polarization. It has been shown previously that this is responsible for the unusual distribution of ferroelectric

domains^{10,18}; here we show that it also has a remarkable impact on the electronic properties of the domain walls.

We choose ErMnO₃ as our model hexagonal manganite, although we expect similar behaviour in the other members of the series. Ferroelectricity in ErMnO₃ emerges at $T_C \cong 833$ K (ref. 19). Six trimerization-polarization domains are formed with a spontaneous polarization $\pm P_z$ pointing along the hexagonal z -axis, as reported previously for YMnO₃ (refs 10,18). In spite of the uniaxial $6mm$ point symmetry the domains possess a nearly isotropic three-dimensional distribution, with a domain size of the order of 1 μm . For our studies, platelets with a thickness of about 200 μm and a lateral extension of typically 1×3 mm² were cut and chemo-mechanically polished with a silica slurry. The platelets were oriented perpendicular to the z - or x -axis so that they possessed an out-of-plane and an in-plane polarization, respectively¹⁸. Samples were investigated by conductive atomic force microscopy (c-AFM) and piezo-response force microscopy (PFM) at ambient conditions.

Figure 1a–c shows c-AFM measurements at different bias voltages. They were obtained on the z -oriented sample in a region remote from any domain wall intersection. The image series reveals that the obtainable c-AFM contrast is bias-dependent. At -1 V, opposite domains with $+P_z$ and $-P_z$ are clearly distinguishable and exhibit different local conductance²⁰ (Fig. 1a). The c-AFM brightness changes across $w_{\text{struct}} \sim 30$ nm at each of the two corresponding domain walls. The change in contrast constitutes a resolution-limited upper bound for the wall width, which is the length scale on which the polarization reverses. At a bias voltage of about -1.6 V, regions separating opposite domains become visible. These regions encase the domain walls centrically and possess a conductance lower than that within the domains. With a further increase of the bias voltage the width of these low-conductance regions increases to $w_{\text{dress}} \sim 140$ nm at -3.5 V. This strikingly exceeds calculated values of the domain wall width generally reported for ferroelectrics^{21–23}.

Thus, we suggest that two characteristic length scales should be distinguished²⁴. First, we have the usual ‘structural wall’ defined by the reversal of the spontaneous polarization and associated with the characteristic displacements of ions. Our measurements indicate that the width $w_{\text{struct}} < 30$ nm. Second, we have an ‘electrically dressed wall’ defined by the region in which the local conductance deviates from that within the bulk domains. The width of this region, $w_{\text{dress}} \sim 10^2$ nm, is bias-dependent

¹Department of Physics, University of California, Berkeley, California 94720, USA, ²Department of Materials Science and Engineering, University of California, Berkeley, California 94720, USA, ³Materials Sciences Division, Lawrence Berkeley National Laboratory, California 94720, USA, ⁴School of Materials Science and Engineering, University of New South Wales, Sydney, New South Wales 2052, Australia, ⁵European Synchrotron Radiation Facility, 6 Rue Jules Horowitz, 38043 Grenoble, France, ⁶Materials Research Laboratory, University of California, Santa Barbara, California 93106, USA, ⁷Department of Materials, ETH Zürich, Wolfgang-Pauli-Strasse, 8093 Zürich, Switzerland, ⁸Zernike Institute for Advanced Materials, University of Groningen, Nijenborgh 4, 9747 AG Groningen, The Netherlands. ^{*}These authors contributed equally to this work. *e-mail: meier@berkeley.edu; jseidel@berkeley.edu.

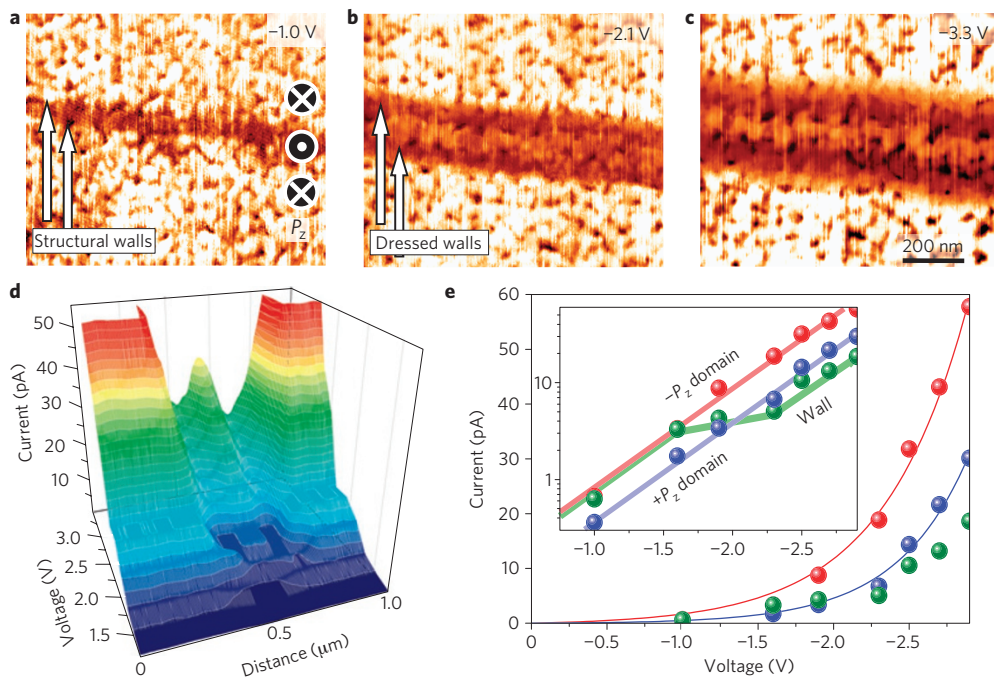


Figure 1 | Bias-dependent domain and domain wall conductance. **a-c**, Local c-AFM image series with different bias voltages across a $+P_z$ domain with adjacent $-P_z$ domains acquired on a z-oriented crystal. Above a threshold of -1.6 V, electrically dressed domain walls become visible and broaden on a further increase of the bias voltage. **d**, Waterfall plot of the measured current cross-sections, showing the evolution of local domain and domain wall width as a function of applied bias. **e**, Extracted local conductance. Whereas the domains show Schottky-like conductance (solid lines represent fits), the conductance of the electrically dressed wall exhibits clear deviations, leading to a crossover around -2 V, as presented in the inset (solid lines are guides to the eye).

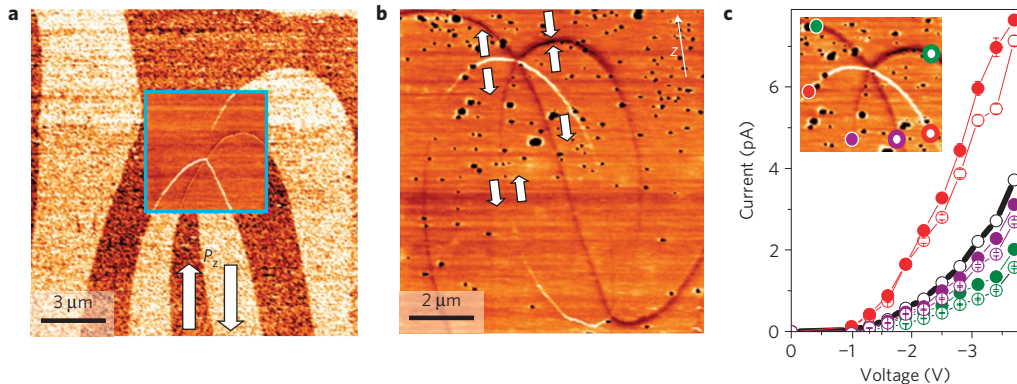


Figure 2 | Anisotropic electrical conductance of ferroelectric domain walls. **a**, PFM image obtained in the yz -plane of an ErMnO_3 crystal. Arrows indicate the direction of polarization. The inset shows a c-AFM image acquired at the same position. Domain walls appear as lines of different brightness on an otherwise homogeneous background, reflecting their different conductance. **b**, c-AFM image of two neighbouring singularities in the yz -plane of ErMnO_3 with polarization directions in-plane as indicated. **c**, Local conductance of the domain walls at the positions indicated in the inset. The data points were derived by fitting a Gaussian profile to cross-sections perpendicular to the wall in **b**. Error bars represent the error of the fit parameter for the maximum value. The domain wall conductance can either be higher or lower than the bulk conductance, varying by more than one order of magnitude.

(Fig. 1d). Our calculations (an analytical solution of the Poisson equation combined with a numerical solution by the finite-element method) indicate that the width of the electrically dressed wall is determined by accumulation/depletion effects of itinerant charge carriers and the resulting nontrivial landscape of conductivity in the vicinity of the domain wall (see Supplementary Information). In Fig. 1e we compare the measured current–voltage characteristics of opposite polarization domains and of the electrically dressed walls separating them. We find that the conductance of the domains can be described by interface-limited Schottky conduction²⁵ (see fits in Fig. 1e), whereas the dressed walls exhibit a more complex current–voltage characteristic, with a plateau from -1.6

to -2.4 V. As consequence, a crossover near -1.9 V occurs (Fig. 1e inset) where the conductance at the dressed walls falls below that of the bulk domains; this is the bias voltage where they become observable.

To understand the phenomenon of electrical dressing of domain walls, we repeated the bias-dependent conductance measurements in the highly anisotropic yz -plane, that is, in the plane of the spontaneous polarization. We find strikingly different conductance behaviour. Figure 2a shows the PFM image of a region in the yz -plane of our ErMnO_3 sample, with the white arrows indicating the orientation of the spontaneous polarization in the plane. The characteristic intersection of six domains described previously^{10,18}

is clearly visible. The inset to Fig. 2a shows the c-AFM data for the same region. It reveals that the domain walls meeting at the intersection have orientation-dependent conductance properties indicated by the different brightness of the c-AFM signal. Figure 2b shows a larger surface area including two intersections. We see that the c-AFM signal along the walls changes smoothly between dark and bright across length scales of a few micrometres. The brightest signal (high conductance) is found at walls where the polarization meets tail-to-tail. In contrast, the darkest signal (low conductance) occurs at walls in the head-to-head polarization configuration. In Fig. 2c we investigate the bias-dependent conductance at points on the six domain walls leading to the upper intersection in Fig. 2b in comparison with the conductance of a bulk domain. The two points in tail-to-tail regions are more conductive (red curves), and the four points in head-to-head regions are less conductive (purple and green curves) than the bulk. In Fig. 3a we present the angular dependence of the normalized local conductance G^{norm} . It is determined according to $G^{\text{norm}}(\alpha) = (I_{\text{wall}}(\alpha) - I_{\text{bulk}})/I_{\text{bulk}}$ by measuring the current $I_{\text{wall}}(\alpha)$ while moving along a ‘domain wall loop’ such as shown in Fig. 2b. Here, α represents the angle between the local wall normal and the direction of the ferroelectric polarization P_z such that $\alpha = 0^\circ$ corresponds to a head-to-head wall and $\alpha = 180^\circ$ to a tail-to-tail wall (see Supplementary Information for details).

We find a distinctly nonlinear relationship between the orientation and the conductance of the domain wall. The difference in conductance at head-to-head and tail-to-tail domain walls can be understood using the schematics and density functional calculations (details are provided in the Supplementary Information) in Fig. 4. At tail-to-tail domain walls (Fig. 4a), the adjacent bound negative charge layers cause an energetically costly divergence in electrostatic potential that must be ameliorated by the accumulation of positive charge. As ErMnO_3 is a p-type semiconductor^{10,20,26} this can be achieved using the readily available mobile hole carriers. At the same time, the variation in electrostatic potential (Supplementary Fig. S3) shifts the Fermi level at the tail-to-tail walls into the broad $\text{O}(2p) - \text{Mn}(3d)$ valence band, where the carrier effective mass is low and the corresponding hole mobility is high. In contrast, at head-to-head walls (Fig. 4c) the bound positive charge layers require negative charge for screening. Because free negative charges (electrons) are scarce in a p-type semiconductor (and any carriers generated by the polar divergence of the wall, as in Fig. 1d, would anyway be required to occupy the narrow, high-effective-mass d_{z^2} band), screening can only be achieved by bound charges such as cation vacancies, which do not contribute to the conduction. At parallel domain walls there is no polar discontinuity and the background conductance of the system is expected (Fig. 4b).

The orientation-dependent spatial distribution of conductivity around charged domain walls in semiconductors was recently predicted in an equilibrium model by Eliseev and colleagues²⁷. Here we apply their model to see if it is consistent with our results. We find, however, that to reproduce our data we need to go beyond the calculation of the equilibrium conductivity, and instead calculate the conductance, based on the actual, non-equilibrium flow of current from the expanded c-AFM tip through the sample, both within and outside the region defining the domain wall.

The local conductivity is proportional to the equilibrium density of holes $p = p_0 \exp(-e\phi/k_B T)$, where p_0 is the density of acceptors and ϕ is the electrostatic potential. As discussed by Eliseev *et al.* in ref. 27 this potential is obtained from Poisson’s equation

$$\phi'' \approx -\frac{e}{\varepsilon} (p - p_0) = -\frac{ep_0}{\varepsilon} \left(\exp\left(-\frac{e\phi}{k_B T}\right) - 1 \right) \quad (1)$$

which determines the variation of the potential in the direction normal to the wall. Integrating equation (1) and using the boundary

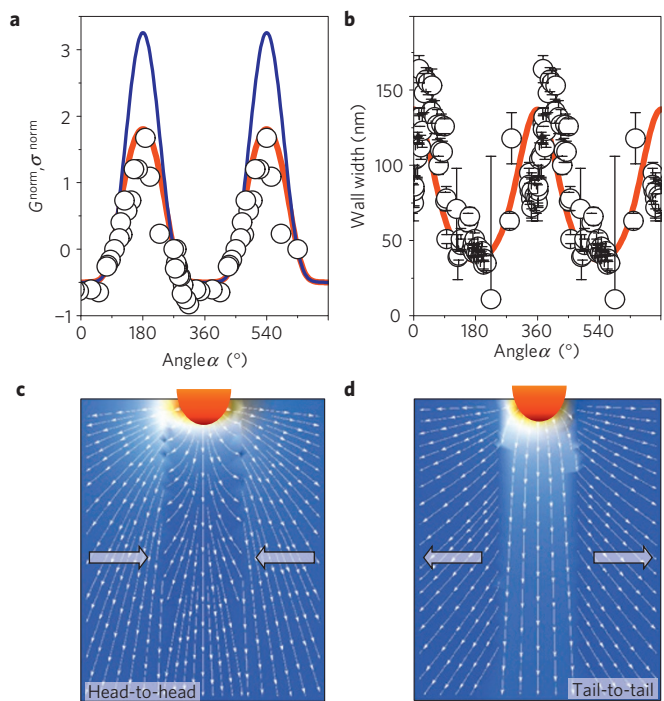


Figure 3 | Angular dependence of the local domain wall conductance.

a, Data points show the angular dependence of the normalized conductance measured along the ‘domain wall loop’ in the centre of Fig. 2b (geometry: see Supplementary Information). $G^{\text{norm}}(\alpha)$ is obtained from a current measurement according to $G^{\text{norm}}(\alpha) = (I_{\text{wall}}(\alpha) - I_{\text{bulk}})/I_{\text{bulk}}$. Extrema are found whenever domain walls are oriented perpendicular to the direction of polarization. The blue and red curves reflect the angular dependence of the calculated normalized conductivity and conductance ($\Pi = 3$ in equation (2)), respectively. **b**, Data points and red line show the measured and calculated (see Supplementary Equation (S4)) angular dependence of the domain wall width, respectively. The data points were derived by fitting a Gaussian profile to cross-sections perpendicular to the wall in Fig. 2b. Error bars represent the error of the fit parameter for the width. A pronounced increase in wall width is observed for the head-to-head domain walls. Note that the data points in **a** and **b** were taken in the range from 0° to 360° and are shown twice for better visual clarity. **c**, Computed spreading of the current injected by the c-AFM tip at a head-to-head domain wall. Owing to the depletion of charge carriers (holes) at the wall the outer environment is more conductive and the current spreads out. **d**, Computed current distribution at a tail-to-tail wall. Although the conductance is locally enhanced, a remarkable leakage out of the domain wall occurs. The white arrows in **c** and **d** indicate the orientation of the polarization along z .

conditions, $\phi(\pm\infty) = 0$ and $\phi'(\pm 0) = \mp(P_z/\varepsilon)\cos\alpha$, we obtain the potential at the domain wall $\phi(0) \equiv \phi_{\text{DW}}$ from

$$\exp\left(-\frac{e\phi_{\text{DW}}}{k_B T}\right) + \frac{e\phi_{\text{DW}}}{k_B T} - 1 = \frac{1}{2} \Pi^2 \cos^2 \alpha \quad (2)$$

where $\Pi^2 = P_z^2/(\varepsilon k_B T p_0)$. The blue curve in Fig. 3a shows the normalized conductivity σ^{norm} at the domain wall with the domain wall conductivity $\sigma_{\text{DW}}(\alpha) \propto \exp(-e\phi_{\text{DW}}/k_B T)$ calculated using this method. The strongly non-sinusoidal angular dependence is indicative of the nonlinear regime of screening of the charged domain walls: for realistic values²⁶— $P_z = 5 \mu\text{C cm}^{-2}$, $\varepsilon = 50\varepsilon_0$, and $p_0 = 2 \times 10^{19} \text{ cm}^{-3}$ —we obtain $\Pi \gg 1$, which precludes a simple linear relation between ϕ_{DW} and the density of bound charges accumulated at the surface of the domain wall, $2P_z \cos\alpha$ (ref. 28).

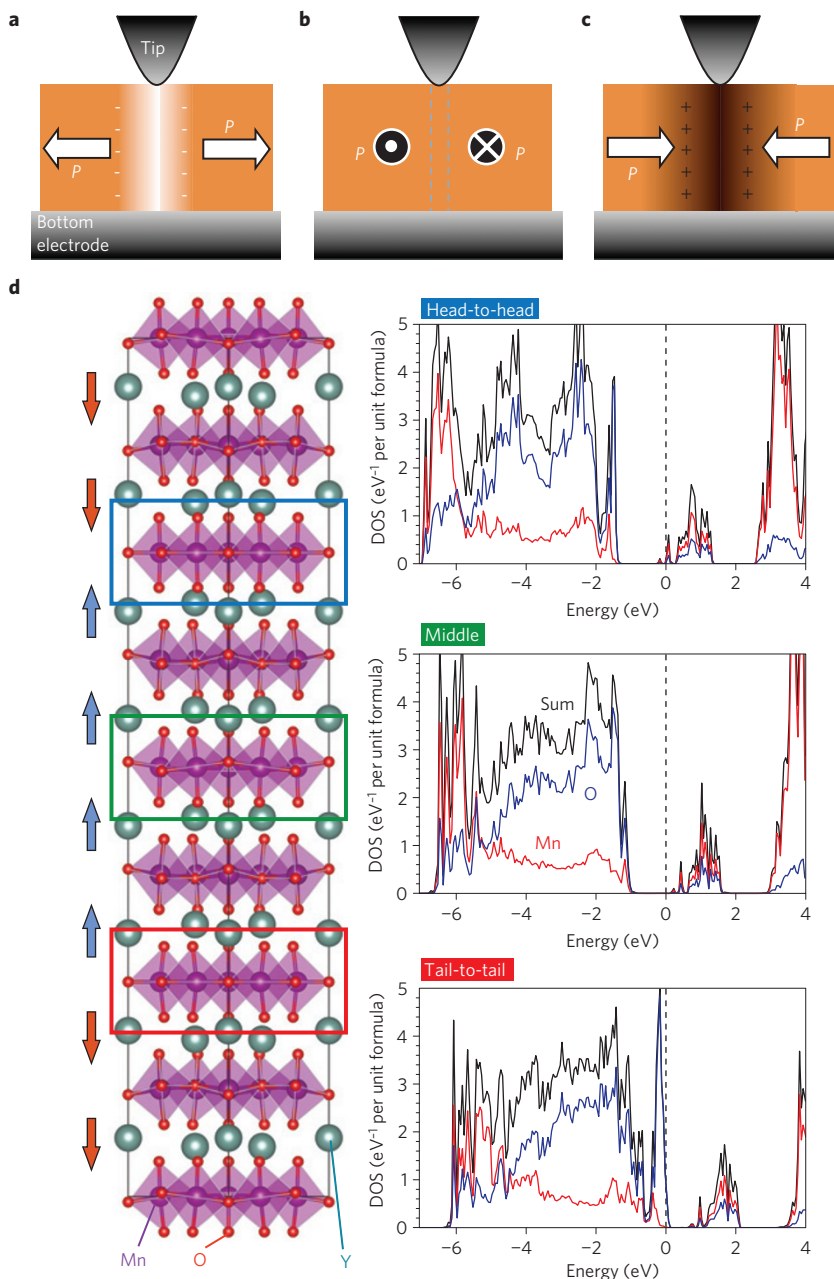


Figure 4 | Electronic structure of charged and uncharged ferroelectric domain walls. **a–c**, Schematic illustrations showing tail-to-tail, side-by-side and head-to-head domain walls, respectively. Here, + and – indicate positive and negative bound charges at the domain wall. A colour scale is used to represent the electrical conductance and the associated hole density (white, high; dark brown, low), see text for details. **d**, Calculated local density of states in the head-to-head (upper right), tail-to-tail (lower right) and domain-centre (middle right) regions of the YMnO₃ supercell shown on the left. The supercell (left) was constructed with four layers of ‘up’ polarized YMnO₃ frozen to the calculated bulk ferroelectric structure, alternating with four layers of ‘down’ YMnO₃. The Mn and O ions in the interface layer were placed at their corresponding paraelectric positions, resulting in a mirror plane at the interface. The black lines in the density-of-states plots indicate the sum of the local density of states, while the blue and red lines show the oxygen and manganese contributions respectively. Note the shift up in energy of the bands from the head-to-head to the tail-to-tail configuration, caused by the gradient in the electrostatic potential.

The significant deviation of the measured normalized conductance $G^{\text{norm}}(\alpha)$ from the calculated conductivity at the domain wall indicates that the injected electric current spreads beyond the domain wall of thickness w_{struct} . Thus, the conductivity of the adjacent region is also probed. To obtain the actual conductance, we solve the continuity equation $\nabla \cdot \mathbf{j} = 0$ for the current $\mathbf{j} = -\sigma \nabla \delta\phi$, where σ is the local conductivity and $\delta\phi$ is the change of potential due to a bias voltage, under the boundary conditions imposed by the tip (see Supplementary Information). This solution reveals a spreading that

is obvious for the head-to-head walls (Fig. 3c). They are surrounded by a more conductive environment owing to the depletion of charge carriers in the wall. However, a strikingly pronounced spreading of the current is also present for negatively charged walls (Fig. 3d) in spite of their locally enhanced conductivity. From the distribution of current we obtain the conductance

$$G(\alpha) \sim \frac{\sigma_{\text{DW}}(\alpha)}{1 + \frac{2r}{w(\alpha)} \ln \frac{\sigma_{\text{DW}}(\alpha) + \sigma_{\text{bulk}}}{2\sigma_{\text{bulk}}}} \quad (3)$$

where σ_{bulk} is the bulk conductivity and $r/w(\alpha)$ is the ratio between the radius of the c-AFM tip and the effective orientation-dependent width $w(\alpha)$ of the domain wall as determined by the accumulation or depletion of holes (see Supplementary Information). Equation (3) directly leads to the normalized conductance (red curve in Fig. 3a), which reproduces the measured data points in Fig. 3a in a strikingly accurate way.

By inserting parameters we can now describe the measured orientation dependence of w_{dress} as seen in Fig. 3b. A rough estimation indicates that $\sim 6 \times 10^{13}$ holes per cm^2 are required (~ 0.1 per formula unit) to completely screen the bound charges at tail-to-tail walls when $P_z = 5 \mu\text{C cm}^{-2}$. For the bulk charge carrier density p_0 this corresponds to a delocalization of screening charges over $\sim 60 \text{ nm}$, which is consistent with the range of values measured for w_{dress} .

In summary, we have demonstrated that the conductance at ferroelectric domain walls in hexagonal ErMnO_3 varies continuously with the orientation of the wall. The variation of the conductance by an order of magnitude between head-to-head and tail-to-tail domain walls is the combined consequence of carrier accumulation and band-structure changes at the walls. Both of these effects were derived theoretically, using phenomenological electrostatic and *ab initio* density functional theory, respectively.

In conventional ferroelectrics such energetically unfavourable head-to-head and tail-to-tail domain walls are usually avoided. However, their presence is enforced in ErMnO_3 because of the protected topology of intersecting domain states in hexagonal manganites^{10,18}. As ferroelectric domain walls, in particular those with no strongly preferred crystallographic orientation as in the present case, can be routinely modified using electric fields, our results suggest a new degree of flexibility for domain boundary engineering²⁹ and oxide-based devices, in which interfaces can be dynamically modified even after assembly into a device architecture.

Received 30 June 2011; accepted 17 January 2012;
published online 26 February 2012

References

- Zubko, P., Gariglio, S., Gabay, M., Ghosez, P. & Triscone, J.-M. Interface physics in complex oxide heterostructures. *Annu. Rev. Condens. Mater. Phys.* **2**, 141–165 (2011).
- Dagotto, E. When oxides meet face to face. *Science* **318**, 1076–1077 (2007).
- Mannhart, J. & Schlom, D. G. Oxide interfaces—an opportunity for electronics. *Science* **327**, 1607–1611 (2010).
- Yamada, H. *et al.* Engineered interface of magnetic oxides. *Science* **395**, 646–648 (2004).
- Ohtomo, A., Muller, D. A., Grazul, J. L. & Hwang, H. Y. Artificial charge-modulation in atomic-scale perovskite titanate superlattices. *Nature* **419**, 378–380 (2002).
- Thiel, S., Hammerl, G., Schmehl, A., Schneider, C. W. & Mannhart, J. Tunable quasi-two-dimensional electron gases in oxide heterostructures. *Science* **313**, 1942–1945 (2006).
- Chakhalian, J. *et al.* Magnetism at the interface between ferromagnetic and superconducting oxides. *Nature Phys.* **2**, 244–248 (2006).
- Mathur, N. D. *et al.* Large low-field magnetoresistance in $\text{La}_{0.7}\text{Ca}_{0.3}\text{MnO}_3$ induced by artificial grain boundaries. *Nature* **387**, 266–268 (1997).
- Gozar, A. *et al.* High-temperature interface superconductance between metallic and insulating copper oxides. *Nature* **455**, 782–785 (2008).
- Choi, T. *et al.* Insulating interlocked ferroelectric and structural antiphase domain walls in multiferroic YMnO_3 . *Nature Mater.* **9**, 253–258 (2010).
- Salje, E. K. H. Multiferroic domain boundaries as active memory devices: Trajectories towards domain boundary engineering. *Chem. Phys. Chem.* **11**, 940–950 (2010).
- Gopalan, V., Dierolf, V. & Scrymgeour, D. A. Defect–domain wall interactions in trigonal ferroelectrics. *Annu. Rev. Mater. Res.* **37**, 449–489 (2007).
- Seidel, J. *et al.* Conduction at domain walls in oxide multiferroics. *Nature Mater.* **8**, 229–234 (2009).
- Farokhipoor, S. & Noheda, B. Conduction through 71° domain walls in BiFeO_3 thin films. *Phys. Rev. Lett.* **107**, 127601 (2011).
- Hill, N. A. Why are there so few magnetic ferroelectrics? *J. Phys. Chem. B* **104**, 6694–6709 (2000).
- Fennie, C. J. & Rabe, K. M. Ferroelectric transition in YMnO_3 from first principles. *Phys. Rev. B* **72**, 100103 (2005).
- Van Aken, B. B., Palstra, T. T. M., Filippetti, A. & Spaldin, N. A. The origin of ferroelectricity in magnetoelectric YMnO_3 . *Nature Mater.* **3**, 164–170 (2004).
- Jungk, T., Hoffmann, Á., Soergel, E. & Fiebig, M. Electrostatic topology of ferroelectric domains in YMnO_3 . *Appl. Phys. Lett.* **97**, 012904 (2010).
- Smolenskii, G. A. & Chupis, I. E. Ferroelectromagnets. *Sov. Phys. Usp.* **25**, 475–493 (1982).
- Wu, W. *et al.* Polarization-modulated rectification at ferroelectric surfaces. *Phys. Rev. Lett.* **104**, 217601 (2010).
- Meyer, B. & Vanderbilt, D. *Ab initio* study of ferroelectric domain walls in PbTiO_3 . *Phys. Rev. B* **65**, 104111 (2002).
- Padilla, J. & Vanderbilt, D. First-principle investigation of 180° domain walls in BaTiO_3 . *Phys. Rev. B* **53**, R5969–R5973 (1996).
- Jia, C.-L. *et al.* Atomic-scale study of electric dipoles near charged and uncharged domain walls in ferroelectric films. *Nature Mater.* **7**, 57–61 (2008).
- Conti, S., Müller, S., Poliakov, A. & Salje, E. K. H. Coupling of order parameters, chirality, and interfacial structures in multiferroic materials. *J. Phys. Condens. Matter* **23**, 142203 (2011).
- Schottky, W. Halbleitertheorie der Sperrschiicht. *Naturwissenschaften* **26**, 843 (1938).
- Subba Rao, G. V., Wanklyn, B. M. & Rao, C. N. R. Electrical transport in rare earth ortho-chromites, -manganites and -ferrites. *J. Phys. Chem. Solids* **32**, 345–358 (1971).
- Eliseev, E. A., Morozovska, A. N., Svechnikov, G. S., Gopalan, V. & Shur, V. Y. Static conductivity of charged domain walls in uniaxial ferroelectric semiconductors. *Phys. Rev. B* **83**, 235313 (2011).
- Mokrý, P., Tagantsev, A. K. & Fousek, J. Pressure on charged domain walls and additional imprint mechanism in ferroelectrics. *Phys. Rev. B* **75**, 094110 (2007).
- Salje, E. K. H. & Zhang, H. L. Domain boundary engineering. *Phase Trans.* **82**, 452–469 (2009).

Acknowledgements

The work at Berkeley is supported by the Director, Office of Science, Office of Basic Energy Sciences, Materials Sciences Division of the US Department of Energy under contract No DE-AC02-05CH1123. The authors acknowledge the following support: by the Alexander von Humboldt Foundation (D.M., J.S.), by the Japan Society for the Promotion of Science Postdoctoral Fellowships for Research Abroad (Y.K.), by the ETH Zürich (N.A.S., M.F.), and by the SFB608 of the Deutsche Forschungsgemeinschaft (M.F.). D.M. is also supported by the National Science Foundation Science and Technology Center (E3S).

Author contributions

D.M. and J.S. initiated this work and conducted the experiments. A.C. and M.M. worked on the phenomenological analysis. K.D., Y.K., and N.A.S. performed the band structure calculations. R.R. and M.F. supervised the research project, and all authors discussed the results.

Additional information

The authors declare no competing financial interests. Supplementary information accompanies this paper on www.nature.com/naturematerials. Reprints and permissions information is available online at www.nature.com/reprints. Correspondence and requests for materials should be addressed to D.M. or J.S.